Geophysical Journal International

A physics-based approach of deep interseismic creep for viscoelastic strike-slip earthquake cycle models

Journal:	*Geophysical Journal International*
Manuscript ID	GJI-S-19-0364.R1
Manuscript Type:	Research Paper
Date Submitted by the Author:	n/a
Complete List of Authors:	Bruhat, Lucile; Laboratoire de Geologie de l'Ecole Normale Superieure; Stanford University, Department of Geophysics
Keywords:	Dynamics and mechanics of faulting < TECTONOPHYSICS, Continental tectonics: strike-slip and transform < TECTONOPHYSICS, Seismic cycle < GEODESY and GRAVITY, Creep and deformation < COMPOSITION and PHYSICAL PROPERTIES, Mechanics, theory, and modelling < TECTONOPHYSICS

submitted to *Geophys. J. Int.*

A physics-based approach of deep interseismic creep for viscoelastic strike-slip earthquake cycle models

Lucile Bruhat[1,2]

[1]*Department of Geophysics, Stanford University, Stanford, California, USA*

[2]*Now at Laboratoire de Géologie, Ecole normale supérieure, PSL Research University, CNRS UMR 8538, 24 rue Lhomond, 75005 Paris, France*

SUMMARY

Most geodetic inversions of surface deformation rates consider the depth distribution of interseismic fault slip-rate to be time invariant. However, some numerical simulations show down-dip penetration of dynamic rupture into regions with velocity-strengthening friction, with subsequent up-dip propagation of the locked-to-creeping transition. Recently, Bruhat & Segall (2017) developed a new method to characterize interseismic slip rates, that allows slip to penetrate up dip into the locked region. This simple model considered deep interseismic slip as a crack loaded at its down-dip end, and provided analytical expressions for stress drop within the crack, slip, and slip rate along the fault. This study extends this approach to strike-slip fault environments, and includes coupling of creep to viscoelastic flow in the lower crust and upper mantle. I employ this model to investigate interseismic deformation rates along the Carrizo Plain section of the San Andreas fault. This study reviews possible models, elastic and viscoelastic, for fitting horizontal surface rates. Using this updated approach, I develop a physics-based solution for deep interseismic creep which accounts for possible slow vertical propagation, and investigate how it improves the fit of the horizontal deformation rates in the Carrizo Plain region. I found solutions for fitting the surface deformation rates that allow for reasonable esti-

mates for earthquake rupture depth and coseismic displacement and improves the overall fit to the data. Best fitting solutions present half-space relaxation time around 70 years, and very low propagation speeds, less than a meter per year, suggesting a lack of creep propagation.

Key words: Creep and deformation – Mechanics, theory, and modelling – Transient deformation – Dynamics and mechanics of faulting – Seismic cycle – Continental tectonics: strike-slip and transform.

1 INTRODUCTION

The earliest models for interseismic deformation described a fault as a single screw dislocation in an elastic half-space, locked to some depth, but slipping at constant rate below (Savage & Burford 1970). Using this simplified model, kinematic inversions of geodetic surface rates have, for decades, been used to estimate the locking depth, presumed to delimit the depth extent of the seismogenic region.

The screw dislocation model lacks physical realism, as shown by the infinite stress concentrations at the dislocation tip. The need for more realistic models called for transitional regions between the fully locked fault and the freely creeping regions. These transitional regions involve some smoothing of the locked to creeping slip distribution, needed to mitigate the stress singularity. As a result, many inversions for interseismic slip rate include some smoothing, or simply add a linear transition from locked to creeping fault (e.g., Flück et al. 1997), whether or not the approach removes the stress singularity. Still, little is known about the physical characteristics of these transitional regions.

A better understanding of the mechanics of the locked-to-creeping transition is even more critical when we consider that the slip-rate distribution might not be stationary in time. While nearly all kinematic inversions of interseismic surface rates make this assumption there is no reason to believe a priori that this is true. Indeed, fully dynamic simulations of earthquake cycles predict that locked-to-creeping transition might evolve significantly during the earthquake cycle. Enhanced dynamic weakening behavior in the velocity-strengthening region can allow dynamic rupture to propagate into the locked-to-creeping transition following the earthquake (Jiang & Lapusta 2016). This behavior had already been observed in conventional rate-state models, where upward penetration of the locked-to-creeping transition occurs over lengths that scale with critical nucleation dimensions (e.g., Hetland et al. 2010; Hetland & Simons 2010; Segall & Bradley 2012; Jiang & Lapusta 2016).

The detection of transient slip behavior during the interseismic cycle, such as slow slip events (Dragert 2001; Obara 2002) or decadal-scale transient events (Mavrommatis et al. 2014), also demon-

strates that a time-invariant interseismic slip-rate distribution is not appropriate. Numerical modeling to reproduce such transient events often exhibit changes in locked-to-creeping transition during the earthquake cycle. Simulations for slow slip events using quasi-dynamic simulations with thermal pressurization have shown that, between large earthquakes, the region of slow slip events gradually propagate into the locked zone (Segall & Bradley 2012). More recently, Johnson et al. (2016) showed that the canonical frictional model with locked asperities of fixed size was inconsistent with GPS-derived deformation in northern Japan. To address this issue, they suggested that locked asperities shrink under surrounding creep during the interseismic period (Mavrommatis et al. 2017). Given the presence of such time-dependent slip events, it appears difficult to support the standard definition of a fixed locked-to-creeping transition.

Bruhat & Segall (2017) recently developed a new method to characterize interseismic slip rates, that allows slip to penetrate up dip into the locked region. This simple model considers deep interseismic slip as a crack loaded at constant slip rate at the down-dip end. It provides analytical expressions for stress drop within the crack, slip, and slip rate along the fault. These expressions allow the expansion of any non-singular slip rate distribution in a combination of Chebyshev polynomials. The simplicity of the method enables inversions for physical characteristics of the fault interface, establishing a first step to bridge from purely kinematic inversions to physics-based numerical simulations of earthquake cycles. When applied to observed deformation rates in northern Cascadia, best fitting models reveal a new class of solutions, where the locking depth migrates up dip with time. Best fitting models there are consistent with a very slow up dip propagation, between 30 and 120 m/yr along the fault.

In this study, I apply this model of propagating deep interseismic creep to strike-slip faults. Unlike Bruhat & Segall (2017), which considered creep propagation in a fully elastic medium, I include here the long-term deformation due to viscoelastic flow in the lower crust and upper mantle. The surface predictions greatly change when including potential viscoelastic deformation and cumulative effect of previous earthquake cycles. Purely elastic models tend to have locking depths greater than the depth of seismicity. Including viscoelastic effects (e.g. Savage & Prescott 1978; Johnson & Segall 2004) allows reasonable fits to interseismic deformation rates with shallower locking depths (e.g. Segall 2010, Section 12.4.2). Obviously, physically motivated models have recently been developed (e.g., Takeuchi & Fialko 2012; Hearn & Thatcher 2015; Lambert & Barbot 2016; Allison & Dunham 2018; Zhang & Sagiya 2018) but are still rare and computationally expensive. I present here a simple method to run quickly kinematic inversions, especially in a Bayesian framework, that provides a better physical description of deep interseismic creep.

I test this new approach by investigating the interseismic deformation rates along the Carrizo Plain

section of the San Andreas fault. The choice for this fault section is twofold. The model I develop is two-dimensional anti-plane strain (infinitely long along strike), so I choose a relative straight and simple part of a major strike-slip system. The Carrizo Plain section segment also motivated work by Jiang & Lapusta (2016) on migrating locking depth. To justify the lack of microseismicity, they suggested that the last event on this section, the M_w 7.9 Fort Tejon earthquake in 1857, could have propagated into the velocity-strengthening region beneath the nominally seismogenic zone. Even 162 years after the last earthquake the stress concentration due to gradients in slip-rate could still be below the region where earthquakes can nucleate.

This study reviews possible models, elastic and viscoelastic, for fitting horizontal surface rates. I improve the model presented in Bruhat & Segall (2017) to account for the coupling between fault creep and viscoelastic flow. Using this updated approach, I develop a physics-based solution for deep interseismic creep which accounts for possible slow vertical propagation, and investigate how it improves the fit horizontal deformation rates for the Carrizo Plain section of the San Andreas fault.

2 METHODS

In this section, I describe the method I develop to compute interseismic deformation rates from viscoelastic earthquake cycle model including up-dip propagation of deep interseismic creep. Surface velocities $\mathbf{v_{horz}}$ result from 1) cumulative effect of viscoelastic earthquake cycle $\mathbf{v_{EQcycle}}$, and 2) the elastic and viscoelastic responses due to interseismic creep, respectively $\mathbf{v_{elcreep}}$ and $\mathbf{v_{vecreep}}$:

$$\mathbf{v_{horz}} = \mathbf{v_{EQcycle}} + \mathbf{v_{elcreep}} + \mathbf{v_{vecreep}} + \alpha + \epsilon \quad \text{with} \quad \epsilon \sim \mathcal{N}(0, \mathbf{\Sigma}). \tag{1}$$

where $\mathbf{\Sigma}$ is the data covariance matrix and α a parameter that accounts for the difference in reference frames for the fault model (anti-symmetric about the fault) and the measured velocities.

2.1 Viscoelastic earthquake cycle model

I first consider the contribution from repeated coseismic slip. Consider a strike-slip fault embedded in an elastic layer of thickness H, overlying a Maxwell viscoelastic half-space (Figure 1). The fault is here considered infinitely long along strike, i.e. it has no along-strike variation. Every T years, an earthquake partly ruptures the fault section. To keep pace with the far-field motion, maximum coseismic displacement is $\Delta u = Tv^{\infty}$, where v^{∞} is the long-term plate rate.

Following Savage & Prescott (1978) and Segall (2010, Sections 6.3 and 12.4.1), I consider the cumulative effect of K regularly spaced earthquakes at $t_{eq} = -kT$, for $k = 0, 1, ..., K$. The surface

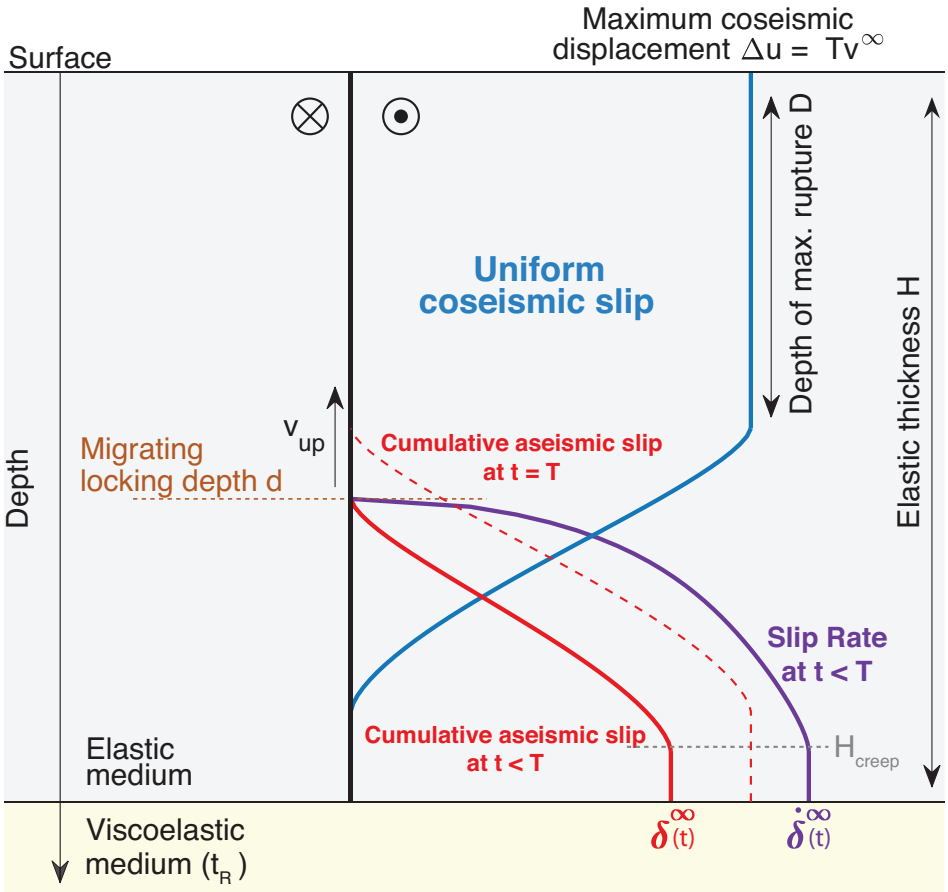

Figure 1. Model set-up for this study. The fault accommodates long-term plate rate v^{∞} in a elastic medium of thickness H, which overlays a viscoelastic half-space characterized by a Maxwell relaxation time t_R. Every T years, an earthquake ruptures the upper part of the elastic crust. Maximum coseismic slip is given by Tv^{∞}. Coseismic rupture is uniform from the surface to depth D, then tapers. During the interseismic period, the deeper part of the fault creeps, pushing the locking depth d up at a speed v_{up}. Interseismic slip evolves from 0 at depth d to $\delta^{\infty}(t)$ at depth H_{creep}. Likewise, slip rates goes from 0 to $\dot{\delta}^{\infty}(t)$ at depth H_{creep}. Slip and slip rates are constant between H_{creep} and the elastic thickness H.The sum of aseismic and seismic slip are set to equal plate motion at all depths.

velocity v_i due to coseismic slip δ_i between z_i and z_{i+1} is then given by:

$$v_i(x,t) = \frac{\delta_i}{\pi t_R} e^{-t/t_R} \sum_{n=1}^{\infty} \frac{G_n(x, z_i, H)}{(n-1)!} \sum_{k=0}^{K} e^{-kT/t_R} \left(\frac{t+kT}{t_R} \right)^{n-1}, \qquad (2)$$

where t is the time since the last earthquake. Positive is for right-lateral strike slip faults. The Maxwell relaxation time t_R of the viscoelastic medium is given by $t_R = 2\eta/\mu$, where η is viscosity and μ shear

modulus. G_n are spatial operators defined by:

$$G_n(x, z_i, H) = F_n(x, z_{i+1}, H) - F_n(x, z_i, H), \tag{3a}$$

$$\text{where} \quad F_n(x, z_i, H) = \tan^{-1}\left(\frac{2nH - z_i}{x}\right) - \tan^{-1}\left(\frac{2nH + z_i}{x}\right). \tag{3b}$$

The cumulative effect $\mathbf{v_{EQcycle}}$ of a coseismic slip distribution described by a distribution of δ_i at depth $z = z_1, .., z_i, .., z_N$ is thus

$$\mathbf{v_{EQcycle}}(x, t) = \sum_{i=1}^{N} v_i(x, t). \tag{4}$$

Expressions for corresponding stress distribution are derived in appendix A.

2.2 Crack models for interseismic creep

Interseismic creep below the locking depth produces elastic deformation at the surface. I here review the method developed in Bruhat & Segall (2017) to describe deep interseismic creep. Consider a 1D crack of length a, extending vertically in the elastic layer and loaded by displacement δ^∞ at the top of the viscoelastic medium (see Figure 1). I follow the same approach of Bruhat & Segall (2017) who expanded the stress drop within the crack in Chebyshev polynomials of the first kind T_i:

$$\Delta\tau(\xi, t) = \mu \sum_{i=0}^{\infty} c_i T_i(\xi), \tag{5}$$

where c_i are the coefficients of the Chebyshev polynomials, and ξ the spatial variable such that $\xi \in [-1, 1]$. ξ is defined as $\xi = 1 - 2z/a$ such that $z \in [0, a]$ and the lower crack end z = 0 is fixed during crack growth. General expressions for stress drop, slip and slip rate distributions for any c_i are given in appendix B.

For a non-singular crack driven at steady displacement, Bruhat & Segall (2017) derived values of the coefficients c_i for $i = 0, 1$. Due to the large number of unknowns already considered in the viscoelastic modeling, I will limit the number of additional parameters to invert from the crack models. In the following inversions, I restrict analysis to the simplest case where for all $i > 1$, $c_i = 0$ and $\partial c_i/\partial t = 0$. This simplification leads to the following stress drop, slip and slip rate distributions:

$$\Delta\tau(\xi, t) = \mu \frac{2}{\pi} \frac{\delta^\infty(t)}{a(t)} \xi \tag{6a}$$

$$\frac{d\Delta\tau}{dt}(\xi, t) = \mu \frac{2}{\pi} \frac{1}{a(t)} \left[\dot{\delta}^\infty(t)\xi + \frac{\dot{a}\delta^\infty(t)}{a(t)}(1 - 2\xi) \right] \tag{6b}$$

$$s(\xi, t) = \frac{\delta^\infty(t)}{\pi} \left[\xi\sqrt{1 - \xi^2} + \arcsin(\xi) + \frac{\pi}{2} \right]. \tag{6c}$$

$$\frac{ds}{dt}(\xi, t) = \frac{\dot{\delta}^\infty(t)}{\pi} \left[\xi\sqrt{1 - \xi^2} + \arcsin(\xi) + \frac{\pi}{2} \right] + \dot{a}\frac{2\delta^\infty(t)}{a(t)\pi}(1 - \xi)\sqrt{1 - \xi^2}. \tag{6d}$$

Bruhat & Segall (2017) set the bottom displacement condition to be that the crack was loaded at constant creep rate v^{∞}. Here I present general expressions that describe displacement and velocity conditions as $\delta^{\infty}(t)$ and $\dot{\delta}^{\infty}(t)$, which are time-dependent boundary conditions coupled to the top of the viscoelastic medium. The slip and slip-rate boundary conditions reflect the transient viscoelastic response of the mantle. Assuming that the crack started propagating after the last major earthquake, I compute $\delta^{\infty}(t)$ and $\dot{\delta}^{\infty}(t)$ to account for viscoelastic flow during this time interval. Details of the derivation of these time-dependent boundary conditions are given in appendix C.

Equation 6d provides an expression for slip rate along the fault. To compute elastic surface rates caused by deep interseismic creep on a fault length Λ, I combine these expressions with homogeneous half-space Green's functions G:

$$\mathbf{v_{elcreep}}(x,t) = \int_{\Lambda} G(x,\xi)\dot{s}(\xi,t)d\xi. \tag{7}$$

I discretize the fault Λ in segments z_i and z_{i+1} for $i = 1,..,N$ such that the above expression can be approximated as discrete:

$$\mathbf{v_{elcreep}}(x,t) \sim \mathbf{G\dot{s}}. \tag{8}$$

2.3 Viscoelastic response from time-varying interseismic creep

In this section, I develop a method to compute analytically the viscoelastic response due to time-varying slip rates below the fully locked region. Consider $\dot{s}(t)$ the slip rate distribution along the fault within the region defined between the depth extent of full earthquake rupture D and the top of the viscoelastic layer H. Following Savage & Prescott (1978) and Segall (2010, Section 12.4.1), the viscoelastic response associated with creep $\dot{s}_i(t)$ at depth z_i, can be written as an infinite sequence of repeating slip events at times t' extending from $-\infty$ to current time t:

$$\hat{v}_i(x,t,z_i) = \frac{1}{\pi}\sum_{n=1}^{\infty}\frac{G_n(x,z_i,H)}{(n-1)!}\int_{-\infty}^{t}\dot{s}_i(t')e^{-(t-t')/t_R}\Big(\frac{t-t'}{t_R}\Big)^{n-1}dt', \tag{9}$$

where G_n is the spatial operator defined in equation 3a. The cumulative effect of a slip rate distribution described by a distribution of slip segments $\dot{s}_i$ between z_i and z_{i+1} for $i = 1,..,N$ is thus

$$\mathbf{v_{vecreep}}(x,t) = \sum_{i=1}^{N}\hat{v}(x,t,z_i). \tag{10}$$

Now consider that the slip rate distribution $\dot{s}(t)$ can be expressed as the sum of the long-term plate motion rate and a time-dependent term. For simplicity, I assume here that prior to the most recent earthquake, i.e. $t < 0$, creep occurred at constant rate, and that only during the current earthquake

cycle, creep is time dependent:

$$\dot{s}(t) = \begin{cases} v^{\infty} + \Delta\dot{s}(t) & \text{when } t \geq 0 \\ v^{\infty} & \text{when } t < 0 \end{cases} \tag{11}$$

The steady part v^{∞} applies to all past earthquake cycles, whereas the time-dependent term corresponds to the present cycle. Substituting this expression into equation (9) gives:

$$\begin{aligned} \hat{v}_i(x,t) &= \frac{1}{\pi}\sum_{n=1}^{\infty}\frac{G_n(x,z_i,H)}{(n-1)!}\int_{-\infty}^{t} v^{\infty}e^{-(t-t')/t_R}\Big(\frac{t-t'}{t_R}\Big)^{n-1}dt' \\ &+\frac{1}{\pi}\sum_{n=1}^{\infty}\frac{G_n(x,z_i,H)}{(n-1)!}\int_{-\infty}^{t} \Delta\dot{s}(t')e^{-(t-t')/t_R}\Big(\frac{t-t'}{t_R}\Big)^{n-1}dt' \end{aligned} \tag{12}$$

The first term corresponds to classical solution for constant creep at speed v^{∞} from Savage & Prescott (1978). The integral can be rewritten as the Gamma function $\Gamma(n)$, which for integer values of n becomes $(n-1)!$. Equation (12) yields

$$\hat{v}_i(x,t) = \frac{1}{\pi}\sum_{n=1}^{\infty} G_n(x,z_i,H)\Big(v^{\infty} + \frac{1}{(n-1)!}\int_{-\infty}^{t}\Delta\dot{s}_i(t')e^{-(t-t')/t_R}\Big(\frac{t-t'}{t_R}\Big)^{n-1}dt'\Big). \tag{13}$$

Because the time-dependent term $\Delta\dot{s}(t')$ is non-zero only during the current cycle, $\Delta\dot{s}(t') = 0$ when $t' \leq 0$, leading to:

$$\hat{v}_i(x,t) = \frac{1}{\pi}\sum_{n=1}^{\infty} G_n(x,z_i,H)\Big(v^{\infty} + \frac{1}{(n-1)!}\int_{0}^{t}\Delta\dot{s}_i(t')e^{-(t-t')/t_R}\Big(\frac{t-t'}{t_R}\Big)^{n-1}dt'\Big). \tag{14}$$

Equation (14) gives the expression of the cumulative effect of viscoelastic flow due to time dependent creep. The first term accounts for constant creep in the region limited by z_i and z_{i+1}. The integral in the second term is calculated numerically. This model is verified against results from Johnson & Segall (2004) who computed slip and slip rate within the creeping region using a boundary element approach (details are given in appendix D). This method reproduces adequately the results from Johnson et al. (2014) except when considering the very early part of the earthquake cycle. The difference originates from Johnson et al. (2014)'s modeling of postseismic deformation. Their model has slip within the creeping region instantaneously after the earthquake in order to match the stress boundary condition, a condition not present in the current formulation. As a result, this method is not be appropriate for modeling afterslip at an early stage of the earthquake cycle. As I intend to study interseismic deformation that is well past the short-term postseismic processes, I conclude that this method is adequate to reproduce viscoelastic response induced by time-dependent creep.

Figure 2 displays slip rate profiles as a function of depth and surface velocity profiles as a function of distance due to elastic and viscoelastic response. These profiles are computed at five times during the interseismic period, and for two normalized relaxation times. Here the creeping region is mod-

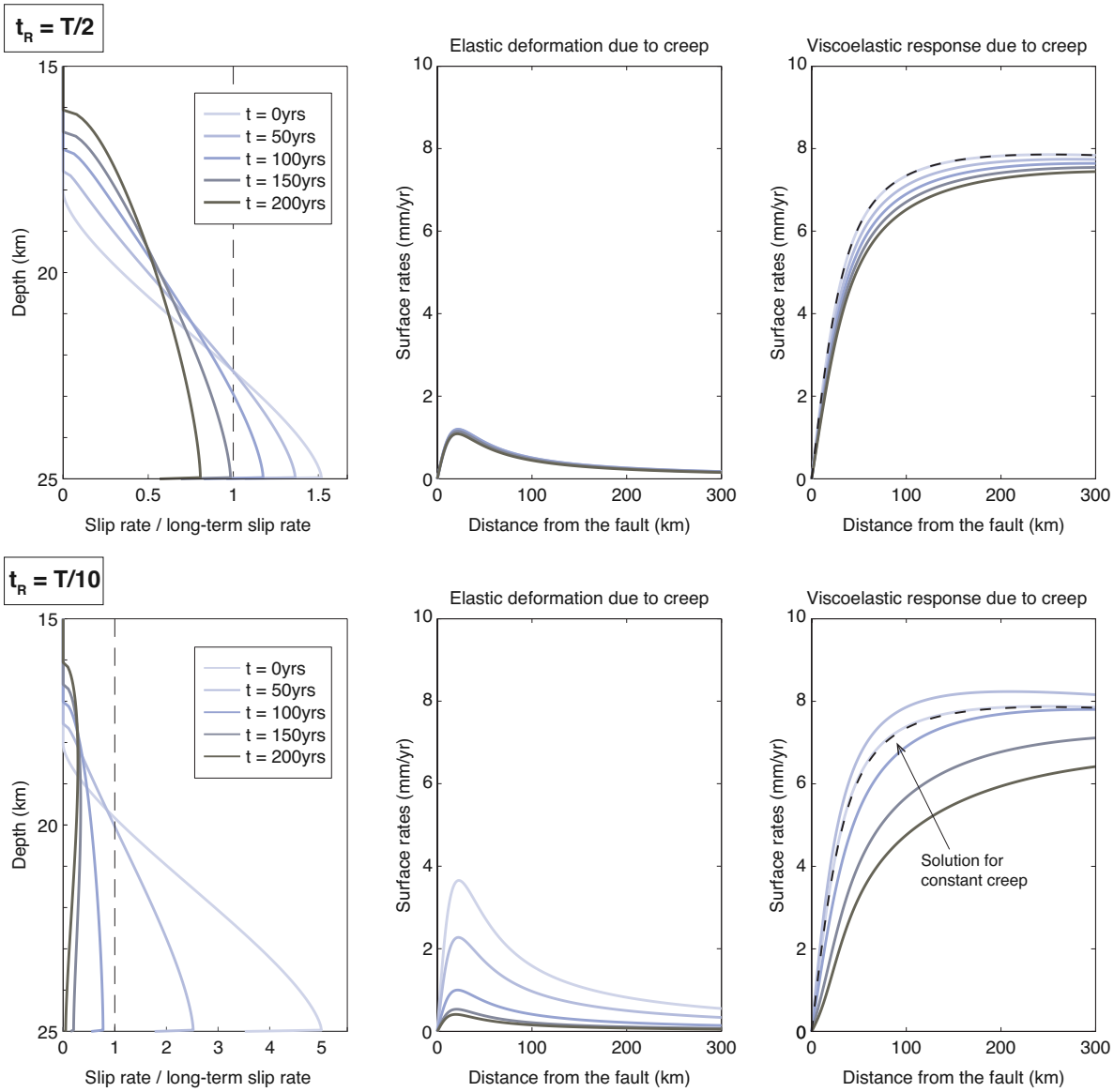

Figure 2. Elastic and viscoelastic deformation induced by time-varying creep when $t_R = T/2$ and $t_R = T/10$. The creeping region is described by a crack lying initially between 18 and 25 km, migrating vertically at 10 m/year. Left panels show the slip rate profiles in the region between the rupture region and the top of the viscoelastic layer. Middle panels show the elastic surface rates caused by interseismic creep. Right panels give the viscoelastic surface rates using equation (14). Dashed back line is the solution for a region creeping at constant rate v^∞.

eled, following section 2.2, by a crack lying initially between 18 and 25 km, migrating vertically at 10 m/year. At $t = 0$ the viscoelastic response is the same as the solution for a region creeping at constant rate v^∞. Depending on the relaxation time, the behavior early in the interseismic period varies. Later in the cycle, the amplitude of the viscoelastic response decreases with time and distance.

3 APPLICATION TO THE CARRIZO PLAIN SEGMENT OF THE SAN ANDREAS FAULT

The previous section developed an improved description of deep interseismic creep which includes the earthquake cycle and response from viscoelastic flow. I now apply this method to investigate geodetic surface velocities across the Carrizo Plain segment of the San Andreas fault.

3.1 Deformation rates

This study considers horizontal interseismic rates in Central California provided by the SCEC Crustal Motion Model Map 4.0 published in Shen et al. (2011). Displacements and velocities were computed from a combination of EDM, GPS, and VLBI data. Stations perpendicular to the Carrizo Plain section of the San Andreas fault are then selected (Figure 3). I exclude stations in the Central Valley to avoid displacements perturbed by the agricultural industry. I finally project the horizontal rates onto a line perpendicular to the fault to obtain a 1D profile of interseismic deformation.

Because this section of the San Andreas fault is too short to fully represent an infinitely long fault, I must account for 3D effects. I use the kinematic block models developed by Johnson (2013) to compute 2D synthetic data along a line perpendicular to the Carrizo Plain section of the San Andreas fault. This model considers the entire extent of the San Andreas fault in Central and Southern California. For this correction only, I assume the San Andreas fault locked to 19 km depth (Smith-Konter et al. 2011) and fully creeping in the northern creeping section. From the surface velocities due to an infinitely-long fault also locked to 19 km, I compute the difference between the 1D and the 2D models; these are considered as a correction for 3D effects, as described in detail in appendix E. This leads to a correction of approximately 1mm/yr, and not symmetric across the fault trace (see Figure A4).

Finally, I correct the data set for the effect of the right-lateral Hosgri fault. This fault system located at the South-Western extent of the considered section presents measured current interseismic deformation. As distant deformation rates strongly affect the fit in a viscoelastic inversion, I correct for the effect of the Hosgri fault. I use results from Johnson & Watt (2012) & Johnson et al. (2014) that indicate a lateral slip rate of 2.6 ± 0.9 mm/yr, considered as a minimum rate for the Hosgri fault given the presence of an active western strand. I take a locking depth of 12 km from Hardebeck (2010) used in UCERF 3 modeling (see Appendix A from UCERF 3 report (Field et al. 2014)). The corrected data are displayed in Figure 3.

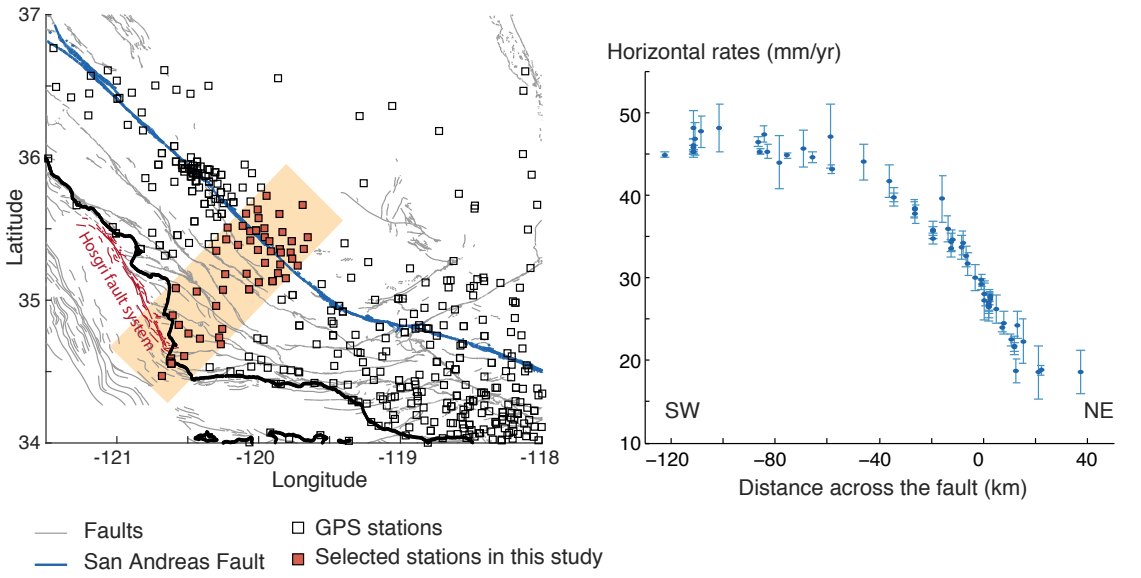

Figure 3. Data set used in this study. Left: Map of central and southern California fault system with selected stations. The San Andreas fault is denoted in blue. Right: Fault parallel component of interseismic velocities relative to the North American plate for the selected stations. The presented rates are corrected for 3D effects and the Hosgri fault.

3.2 Current knowledge of fault coupling and earthquake characteristics

Paleoseismic studies provide constraints on the surface coseismic slip. Although earliest measurements suggested surface displacements up to 10 m along the Carrizo Plain segment (Sieh 1978), these estimates have been reevaluated since to lower estimates, around 5–7 m (Zielke et al. 2010; Scharer et al. 2014). In this study, I impose the coseismic slip distribution (Figure 1). For simplicity, I will consider that the coseismic displacement is constant with depth down to the full rupture depth D recognizing that in fact it must be tapered. A reasonable estimate for the maximum coseismic displacement in this study will be 8 m.

Classical dislocation models define the locking depth as the greatest depth of slip deficit. In this study, the locking depth is defined as the upper (shallowest) limit of the interseismic slip rate (Figure 1). Since I assume that the sum of aseismic and coseismic slip are set to equal plate motion at all depths, the upper (shallowest) bound of the locking depth is given by the extent of the maximum coseismic displacement. Across the Carrizo segment of the San Andreas fault, numerous studies have estimated over the past decades the locking depth, using different modeling approach from elastic dislocations to fully numerical models. In 2010, a Southern California Earthquake Center (SCEC) workshop compiled these estimates through an exercise where participants were asked to fit the geodetic surface rates using whatever method they preferred (see https://www.scec.org/workshops/2010/gps-

ucerf3/index.html). The mean locking depth estimated from nine independent analyses of the same geodetic data set was then 16.7 $\pm$ 2.2 km. Likewise, using a geodetically constrained semi-analytic dislocation model for the entire Southern California fault system, Smith-Konter et al. (2011) found locking depths around 18.7 $\pm$ 2.0 km across the Carrizo Plain segment. In this study, I consider that a reasonable estimate on the locking depth around or less than 16.7 km.

Geological studies, such as Noriega et al. (2006), provide bounds on long-term plate motion rate v^{∞} around 30–37 mm/yr at the Carrizo Plain segment. More recently, using a suite of inversions with four kinematic models, some of them including viscoelastic flow, Johnson (2013) found that slip rates range from 29 to 37 mm/yr for the Carrizo segment of the San Andreas Fault. In this study, I bound v^{∞} to 29–37 mm/yr.

Records of microseismicity also provide information on fault coupling. Using the earthquake catalog from Lin et al. (2007), Smith-Konter et al. (2011) examine seismicity profiles along the San Andreas fault to define the thickness of the seismogenic layer. Across the Carrizo Plain segment, microseismicity is first estimated to extend down to at 14-16 km. Using the SCSN relocated earthquake catalog for Southern California, downloaded from http://scedc.caltech.edu/research-tools/alt-2011-dd-hauksson-yang-shearer.html (Lin et al. 2007; Hauksson et al. 2012), most of the seismicity is located at depths 8–12 km, but extends to as much as 18 km. This helps constrain reasonable upper bounds on the elastic thickness H and the current locking depth.

3.3 Slip rate inversions

In this section, I describe the inversions that will be carried out in the next section. Surface velocities $\mathbf{v_{horz}}$ results from the cumulative effect of viscoelastic earthquake cycle $\mathbf{v_{EQcycle}}$, and the elastic and viscoelastic responses due to interseismic creep, respectively $\mathbf{v_{elcreep}}$ and $\mathbf{v_{vecreep}}$:

$$\begin{aligned} \mathbf{v_{horz}} &= \mathbf{f}(H, D, t_R, \Delta u, v_{\infty}, d, v_{up}, H_{creep}, \alpha), \\ &= \mathbf{v_{EQcycle}} + \mathbf{v_{elcreep}} + \mathbf{v_{vecreep}} + \alpha + \epsilon \quad \text{with} \quad \epsilon \sim \mathcal{N}(0, \mathbf{\Sigma}) \quad \text{(Equation (1)).} \end{aligned}$$

where $\mathbf{\Sigma}$ is the data covariance matrix and α a parameter that accounts for reference frame offset. Equations for $\mathbf{v_{EQcycle}}$ are given in section 2.1. $\mathbf{v_{elcreep}}$ relates to the unknown vector of slip-rates $\dot{\mathbf{s}}$ via elastic homogeneous half-space Green's functions $\mathbf{G}$. Equations for the viscoelastic response $\mathbf{v_{vecreep}}$ are given in section 2.3 using expressions for interseismic slip rates given in section 2.2. Inversions search for the elastic thickness H, the rupture depth D, the present-day position of the locking depth, defined by the top of the creeping region d, the long-term plate motion rate v^{∞}, the viscoelastic relaxation time t_R, and the maximum coseismic displacement Δu, related to the earthquake recurrence time T. To account for the possibility of a region of constant creep at the transition between

Parameter	Symbol	Minimum	Maximum
Maximum depth of full earthquake rupture, km	D	5	10
Long-term fault slip rate, mm/yr	v^{∞}	29	37
Elastic thickness, km	H	18	100
Half-space relaxation time, years	t_R	0	500
Coseismic displacement, m	Δu	4	8
Present-day locking depth, km	d	D	H
Depth of constant creep, km	H_{creep}	d	H
Recurrence time, m/yr	T	$\Delta u/v^{\infty}$	$\Delta u/v^{\infty}$
Propagation speed, m/yr	v_{up}	(d-D)/(T-162)	(d-D)/(T-162)
Time since 1857 earthquake, years	t	162	162 (fixed)
Block motion, mm/yr	α	none	none

Table 1. A priori bounds for MCMC inversions

the elastic and the viscoelastic region, I invert for the bottom depth of the creeping region H_{creep} (see Figure 1). Between H_{creep} and H, the fault slips at the constant speed $\dot{\delta}^{\infty}$ defined in section 2.2.

Finally, in order to be consistent with microseismicity data, I will consider solutions whose peak in stress rate lies in the same region as the current seismicity (between 8–13 km). This is an important point in this inversion. This updated model allow us to derive the distribution of shear stress rate within the creeping region. While this inversion is directed by horizontal geodetic rates, I assume that the highest rate should coincide with the location of maximum shear stressing rate, which is indicated by the region of largest moment release from the microseismicity.

The coseismic slip distribution is defined as followed. From the surface to the full rupture depth D, the coseismic slip distribution is equal to the maximum coseismic displacement Δu. To ensure that at the end of the cycle, slip along the entire fault is equal to the maximum coseismic displacement, the coseismic slip distribution between D and H_{creep} is defined as the complement of the aseismic slip distribution at the end of the cycle (see Figure 1). In other words, I not only integrate up to the current time, but also to the end of the cycle, $T = \Delta u/v^{\infty}$. Likewise, I bound the migration speed v_{up} such that slip in the elastic region is equal to Δu at the end of the cycle. The creeping region must reach the down dip limit of the coseismic region at the end of the earthquake cycle:

$$v_{up} = \frac{d - D}{T - 162}. \tag{16}$$

This study aims at developing inverse methods to test different models of interseismic deformation, accounting in some cases for propagating deep creep. Since I consider viscoelastic deformation I estimate at least the rupture depth D, the elastic thickness H, the viscoelastic relaxation time t_R, the

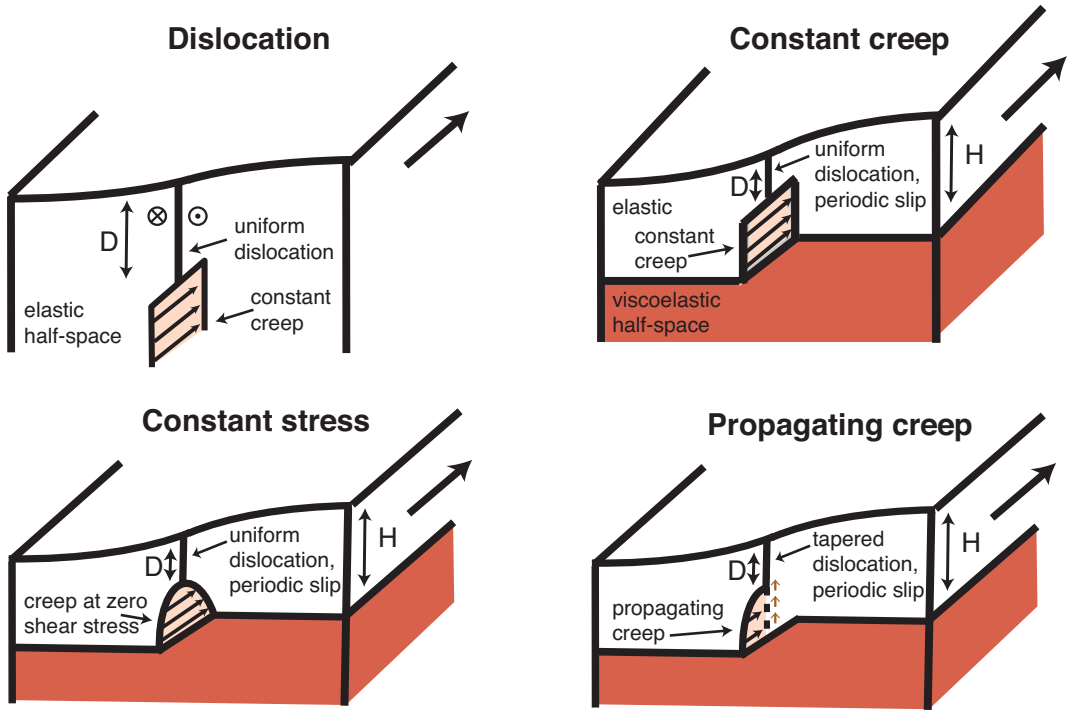

Figure 4. Models for interseismic creep considered in this study. Details are summarized in Table 2.

coseismic displacement Δu, the long-term plate motion rate v^{∞}, and α. When considering models with propagating deep interseismic slip, I also invert for the locking depth d, and deduce the propagation speed v_{up}. I employ Markov Chain Monte Carlo (MCMC) methods for the inversions. MCMC algorithms efficiently estimate the maximum-likelihood solution and enable the construction of posterior distributions. I assume that the loading time t that appears in equations (6) is fixed at 162 years, since the last earthquake occurred in 1857. Depending the inversions, prior knowledge about the other model parameters will be included. A priori bounds are summarized in table 1.

4 RESULTS

In this section, I present the results of this inversions to fit geodetic rates across the Carrizo Plain section of the San Andreas. I first found best fitting solutions for classical inversions that consider either the fault to be a single dislocation in a fully elastic medium, or models that include a region of steady creep above a viscoelastic region. I also consider solutions from the boundary element method developed by Johnson & Segall (2004). I finally apply the method I developed including propagating deep interseismic creep. Different creep models are sketched in Figure 4.

Inversions details are summarized in Table 2, and best fitting parameters and confidence intervals are given in Table 3. Recall that due to the skewness of some posterior distributions, the best fitting

Type	Label	Description
Elastic	Dislocation	Single dislocation in elastic half-space
Viscoelastic	Constant creep	Model from Savage & Prescott (1978)
		Creeping region slipping at constant speed v^{∞}
Viscoelastic	Constant stress	Model from Johnson & Segall (2004)
		Creeping region slipping at constant resistive stress
Viscoelastic	Propagating creep	This study
		Creeping region migrating vertically

Table 2. Inversion descriptions

solution might not lies within the 95% confidence interval. The results of the inversions are summarized in Figure 5. The posterior distributions of the full rupture depth D, the elastic thickness H, the coseismic displacement Δu, the relaxation time t_R, the recurrence time T, the locking depth d, and propagation speed v_{up} are displayed for the four inversions. Best fits and log-likelihood distributions are shown in Figure 6.

I first perform classical inversions to explain the deformation rates across the Carrizo Plain segment. Best fitting parameters will provide insights on expected fault parameters inferred from this set of data, before launching more complicated inversions. I first consider a single dislocation within an elastic medium ($d = D$). Because I only invert for the maximum depth of uniform coseismic slip and long-term velocity in this model, resulting distribution are only shown for the depth D. The inverted locking depth is 10 km and long-term plate rate v^{∞} 30.1 mm/yr.

The remaining inversions consider the fault to be embedded in an elastic layer lying over a viscoelastic medium. Inverted parameters are the coseismic uniform depth D, elastic thickness H, relaxation time t_R, coseismic displacement Δu and v^{∞}. The first inversion considers creep at constant velocity v^{∞} between D and H (as in Savage & Prescott 1978). Best fitting solutions indicate rupture depth of 10 km and elastic thickness of 18 km. Maximum coseismic displacement reaches 8 m. This model favors a short relaxation time, of around 39.2-55 years. Recurrence time T ranges from 216.8 to 226.5 years. The second inversion assumes the creeping region to slip at constant resistive stress. This is the model developed by Johnson & Segall (2004). Best fitting parameters also reaches 10 km for D and 8 m for Δu. Unlike the previous inversion, this model infers slightly higher values for the elastic thickness H, between 17.6 to 19.4 km, and shorter recurrence time, around 215 years. The estimated relaxation time t_R is two to three times higher than the one in the previous inversion.

Finally, I perform the inversion using my model. Uniform rupture depth is estimated between 9.1 and 10.3 km. Estimates of elastic thickness vary from 17.1 to 21.5 km. Coseismic slip is in the range

Model	Dislocation		Constant creep		Constant stress		Propagating creep	
Parameter	Best fit	95% Conf.	Best fit	95% Conf.	Best fit	95% Conf.	Best fit	95% Conf.
D, km	10.0	9.9-10.0	10.0	9.9-10.0	10.0	9.4-10.2	10.0	9.1-10.3
v^{∞}, mm/yr	30.1	29.5-30.7	34.7	33.7-36.4	37.0	36.6-37.1	32.8	32.8-37.6
H, km			18	17.9-18.2	18.0	17.6-19.4	18.2	17.1-21.5
t_R, years			45.5	39.2-55.0	101.0	99.8-118.4	70.2	48.4-111.0
Δu, m			8.0	7.3-8.2	8.0	7.4-8.1	7.8	6.9-8.3
d, km							10.0	9.2-10.5
H_{creep}, km							18.2	15.6-21.3
T, years			230.5*	216.8-226.5*	215.0*	203.4-219.5*	234.0*	209.6-221.2*
T/t_R			5.1*	4.1-5.5*	2.1*	1.8-2.0*	3.3*	2.0-4.3*
v_{up}, m/yr							0.43*	0.0-8.5*

Table 3. Inversion results for all the tested models. Parameters with an asterisk are not inverted, but inferred using the relations given in Table 1.

6.9 to 8.3 m. Recurrence time lies between 209 and 221 years. Current locking depth lies between 9.2 and 10.5 km, co-located at the location of most of the microseismicity. Finally, rates for propagating creep vary between 0 and 8.5 m/years. The relaxation time of the best fitting solution lies at 70.2 years, varying from 48.4 to 111.0. Figure A5 presents the posterior distributions for parameters estimated in the propagating creep inversion, and the resulting propagation speed. I observe a positive correlation between the relaxation time t_R, the elastic thickness H and the depth of constant creep H_{creep}. When focusing on the propagation speed v_up, there does not seem to be any strong correlation with the other inversion parameters. The sudden decrease in relaxation time between the model developed by Johnson & Segall (2004) and mine does not seem to be solely related to the addition of the propagating creep.

Although I found differences in parameters between the three viscoelastic earthquake cycle inversions, Figure 6 shows that the differences in fit are limited. This improved model shows, however, a better range for the likelihood, compared to all other inversions. I also compute the deviance information criterion (DIC) (Spiegelhalter et al. 2002) to compare the fits. The deviance D(m) is defined as

$$D(m) = -2\log(p(d|m)) + C \tag{17}$$

where d is the data, m the unknown parameters, $p(y|m)$ the likelihood and C a constant that later cancels. The influence of the effective number of parameters is given by the difference between the

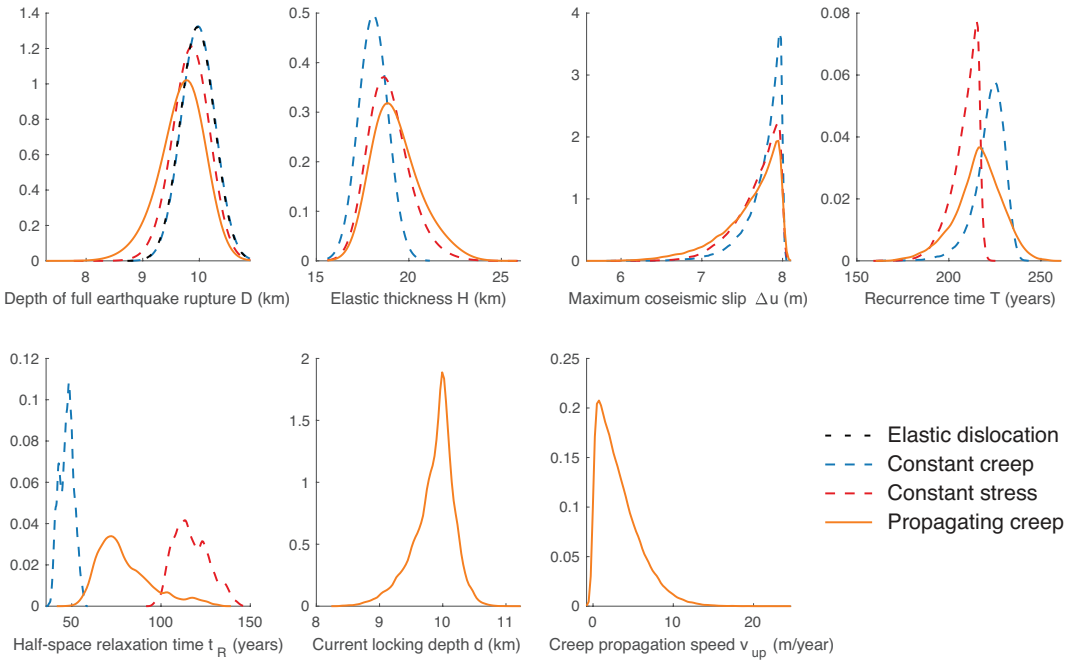

Figure 5. Posterior distributions for the depth of maximum coseismic slip D, the elastic thickness H, the amount of maximum coseismic slip Δu, the half-space relaxation time t_R, the recurrence time T, and, for this model specifically, the distribution of the current locking depth d and propagation speed of deep interseismic slip v_{up}. See Figure 1 for a review of the different parameters.

expectation of the deviance $\bar{D}(m)$ and the deviance of the expectation of m:

$$p_D = \bar{D}(m) - D(\bar{m}). \tag{18}$$

The deviance information criterion (DIC) is then computed as followed:

$$DIC = D(\bar{m}) + 2p_D. \tag{19}$$

The DIC is a way of measuring model fit, similar to Akaike information criterion (AIC), but for MCMC solutions. Models with lower DIC give the best estimated solutions. In this study, although I increased the number of parameters, my improved model has a DIC lower than all the other inversions, as shown in Figure 6.

5 DISCUSSION

I investigated models that include viscoelastic flow and deep interseismic creep to explain the deformation rates across the Carrizo Plain section of the San Andreas fault. I improved the method develop by Bruhat & Segall (2017) to account for the coupling between the viscoelastic half-space and time-dependent interseismic creep. I propose a model with a coseismic region with constant coseismic slip

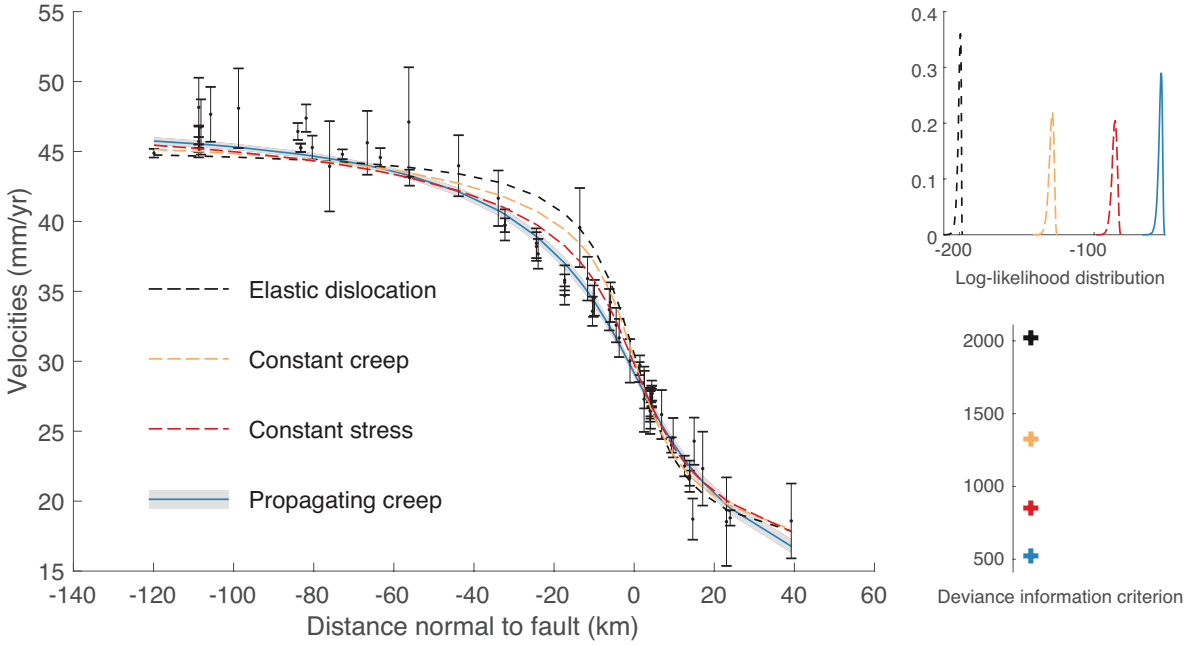

Figure 6. Best fitting models, log-likelihood distributions and corresponding deviance information criteria. Although the difference is small, this propagating creep model fits better the data set compared to other models. Recall that the data were corrected for 3D effect and the effect of the Hosgri fault.

down to 10 km, then slowly tapering down to 15-20 km (Figure 7). The region of uniform coseismic rupture, down to ≈10 km is followed by a transitional region, where creep lies between the top of the viscoelastic layer and the apparent locking depth, and potentially can migrate vertically at speeds up to 10 m/year. This model exhibits positive stress rate within the same region than the current microseismicity. This results show that this model might explain the surface rates across the Carrizo Plain section of the San Andreas fault.

Compared to the model with constant creep from Savage & Prescott (1978) and the boundary element model developed by Johnson & Segall (2004), I present a kinematic model that is much more efficient computationally and allow the spatial migration of the creeping region during the earthquake cycle. I derived analytical expressions for this to compute the viscoelastic response due to time-dependent creep. Although this model remains kinematic, it provides physical insights into the transitional region between the locked region and the top of the viscoelastic medium.

Note that the best fitting solutions from this model have very low propagation speeds, less than a meter per year, as shown in Figure 8, advocating for the lack of creep propagation. As a result, the difference in fit with the model developed by Johnson & Segall (2004) where creep occurs at constant creep, does not seem to be caused by the additional creep propagation. The model I developed, inde-

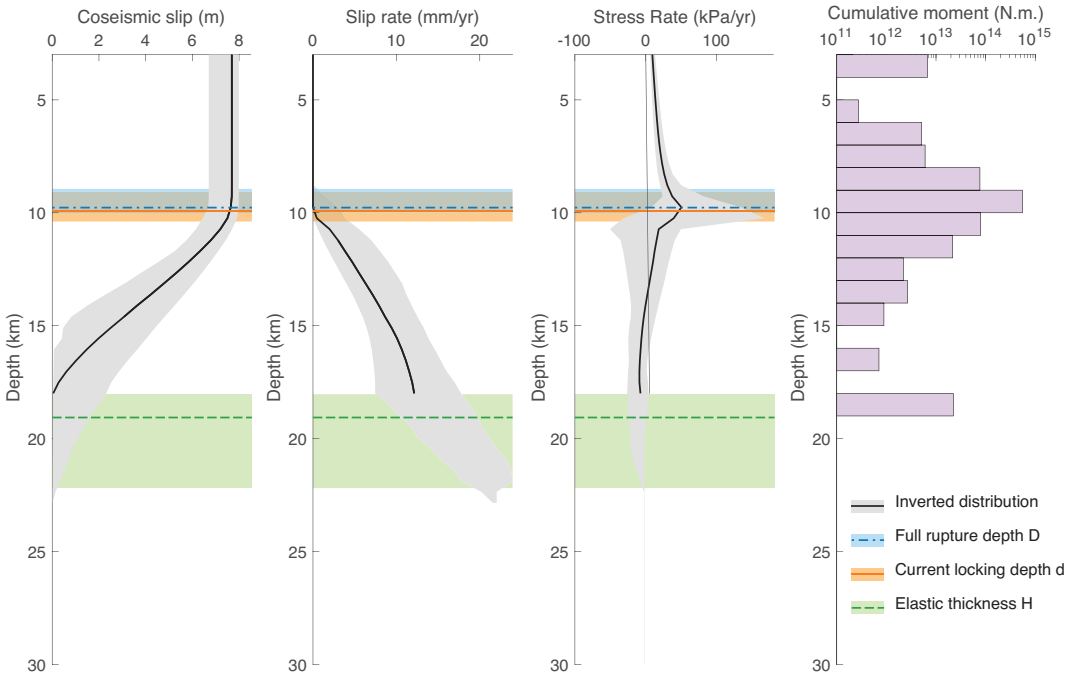

Figure 7. Distribution of coseismic slip, slip rate, stress rate, D, d and H for this improved model. Median solutions are indicated in bold lines, the 2-σ uncertainties are given by the shaded regions. I compare the obtained stress rate distribution to the cumulative moment from microseismicity between 1981 and 2016 along the Carrizo Plain (Lin et al. 2007; Hauksson et al. 2012).

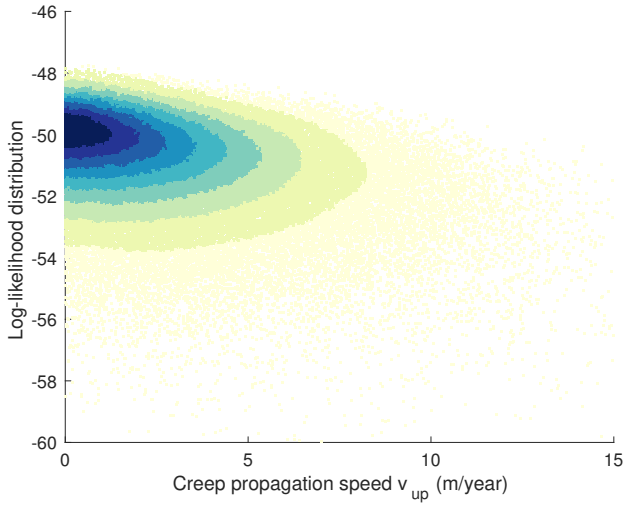

Figure 8. Density plot of the posterior distribution of the creep propagation speed against the log-likelihood. A lower log-likelihood indicates a better fit. In this inversion, while I allow the possibility for vertical migration of the locking depth, the best fitting solutions converge toward a solution which is not migrating.

pendently from the propagation, seems to provide a more flexible solution for creep rate distribution in the transitional region, leading to a systematic better fit.

All prior models assumed constant coseismic displacement along depth, meaning that the earthquake rupture would abruptly stop as it reaches the depth D. A sudden earthquake arrest is however probably unlikely. Most slip inversions assume spatial smoothing between patches of high and low slip for instance. The model I present here includes a more realistic transitional region below the depth of uniform rupture D. It allows the presence of a transitional region where tapered coseismic slip and migrating interseismic creep are co-located. Recent numerical studies have hinted the possibility for such deeper partial coseismic ruptures (Jiang & Lapusta 2016) due to enhanced weakening mechanisms. Although partial rupture add an extra degree of complexity when describing the transition between the locked and the creeping regions, such models improve significantly the physical representation of the transitional region and the overall fit, as shown in Figure 6.

All the considered models assume an instantaneous characteristic rupture every T years. Although, the cumulative response of the underneath viscoelastic medium to each characteristic earthquake is acknowledged, most of them neglect time-dependent afterslip and more generally postseismic deformation. Postseismic slip could account for a significant part of the slip happening within the creeping region. Only the boundary element model developed by Johnson & Segall (2004) considered instantaneous slip in the region between D and H, which might be assimilated as a partial deep rupture, but does not evolve with time. As the deep region of the elastic layer slips post-seismically, it also feeds and amplifies the response of the viscoelastic medium. This additional time-dependent behavior from the postseismic response is completely ignored in any of this viscoelastic modeling.

The variability of the typical-earthquake characteristics might also affect the long-term viscoelastic cycle model. Although the San Andreas Fault has been quiet in this region since 1857, paleoseismic studies have shown that most precedent events displayed lower surface-breaking displacements, as well as shorter recurrence time intervals (Akciz et al. 2009, 2010; Scharer et al. 2014) These studies suggest that there is no "characteristic" earthquake along the Carrizo Plain segment, and that, as a result, the 1857 event might be a rare larger event. Note that the corollary would also suggest smaller coseismic displacements in the geodetic inversions.

Nevertheless, I developed a model which allows crack propagation that considers the coupling between the viscoelastic half-space and the creeping region. In particular, I extended the models from Bruhat & Segall (2017) to compute viscoelastic surface rates caused by time-dependent slip rates along the fault. Using this improved model, I found solutions for fitting the surface deformation rates that allow for reasonable estimates for earthquake rupture depth and coseismic displacement. Above the viscoelastic half-space, deep interseismic slip might be migrating vertically at rates up to 10 m/year,

slowly unlocking the deepest region of the elastic crust. I present a model that could be used as a first step to explain the discrepancy between geodetically-derived locking depths and microseismicity along the San Andreas fault. The observation of deep microseismicity and tremors suggests indeed that there is at least some fault slip well below the nominally locked part of the fault (Nadeau & Guilhem 2009; Shelly 2010). However, since the propagation velocity is very small, less than 1 km in 100 years, it is highly likely that the creep migration, if real, could not be currently detected given the geodetic data temporal span and the still large uncertainties on the locking depth along the San Andreas fault.

Likewise, I tested this method on a simple data set that used averaged temporal deformation. The addition of a possible time-dependent behavior calls for the use of time-dependent data, that would highlight the characteristics of migrating speed. Future work should consider the use of additional data sets, such as microseismicity, repeating earthquakes, and tremor locations, to study and better constrain this behavior in fault systems. As observations of time-dependent deformation during the interseismic period, or even before large events, become more common, this type of inversion method would become more and more necessary.

While this study focused on the Carizzo plain section of the San Andreas fault, the approach could be easily expended to other strike-slip faults. Current work on the North Anatolian fault have shown for instance that the long-term deformation rates seem constant through the interseismic period, which could suggest the lack of migrating creep (Hussain et al. 2018). The study from Jiang & Lapusta (2016), which actually first mentioned the possibility of a migrating locking depth, looked at microseismicity pattern in large strike-slip fault segments to estimate whether the locking depth could have been pushed further at depth after large earthquakes. These locations could serve as starting point for further evaluating deep interseismic creep.

The first and most obvious application of my method is to provide a physics-based tool for kinematic inversions that remains simple to use, but still allows vertical migration of the creeping region in a viscoelastic earthquake cycle modeling. Nonetheless, this method could also be used as a verification tool for more elaborated physics-based fully-numerical modeling. While I recognize that dividing the crust in a elastic medium of constant elastic moduli overlying a viscoelastic half-space remains a simple model that strongly differs with recent physically motivated models (e.g., Takeuchi & Fialko 2012; Hearn & Thatcher 2015; Lambert & Barbot 2016; Allison & Dunham 2018; Zhang & Sagiya 2018), such methods for modeling the crust are still wildly used in kinematic inversions. Results from fully-numerical models should be verified against various approach of kinematic inversions, such as the one developed here. For instance, when Allison & Dunham (2018) finds that even the brittle-ductile transition evolves with cumulative earthquake cycle, it would be really interesting to invert the surface deformation rates they produce with the method I developed here. As screw dislocation arctangents

remain still fairly ubiquitous (Meade et al. 2013; Wright et al. 2013), being able to pinpoint the components of interseismic deformation rates to actual physical characteristics using knowledge from both the kinematic inversions and the fully-numerical models would be an encouraging step forward.

ACKNOWLEDGMENTS

I would like to thank Paul Segall for discussions and guidance through this work, and Kaj Johnson for providing me his viscoelastic code. I also thank the editor Eiichi Fukuyama, Tim Wright and an anonymous reviewer for their constructive comments. This work was supported by the Southern California Earthquake Center (Award #17136). GPS rates were provided by the SCEC Crustal Motion Model Map (Shen et al. 2011) and are available at https://goo.gl/gsHgQr. Codes for crack and viscoelastic modeling are available on https://github.com/lucilebruhat/.

REFERENCES

Akciz, S. O., Grant Ludwig, L., & Arrowsmith, J. R., 2009. Revised dates of large earthquakes along the Carrizo section of the San Andreas Fault, California, since A.D. 1310 30, *Journal of Geophysical Research*, **114**(B1), B01313.

Akciz, S. O., Ludwig, L. G., Arrowsmith, J. R., & Zielke, O., 2010. Century-long average time intervals between earthquake ruptures of the San Andreas fault in the Carrizo Plain, California, *Geology*, **38**(9), 787–790.

Allison, K. L. & Dunham, E. M., 2018. Earthquake cycle simulations with rate-and-state friction and power-law viscoelasticity, *Tectonophysics*, **733**, 232–256.

Bilby, B. A. & Eshelby, J. D., 1968. Dislocations and the theory of fracture, in *Fracture, an advanced treatise*, pp. 99–182, Academic Press New York and London.

Bruhat, L. & Segall, P., 2017. Deformation rates in northern Cascadia consistent with slow up dip propagation of deep interseismic creep, *Geophysical Journal International*.

Dragert, H., 2001. A Silent Slip Event on the Deeper Cascadia Subduction Interface, *Science*, **292**(5521), 1525–1528.

Field, E. H., Arrowsmith, R. J., Biasi, G. P., Bird, P., Dawson, T. E., Felzer, K. R., Jackson, D. D., Johnson, K. M., Jordan, T. H., Madden, C., Michael, A. J., Milner, K. R., Page, M. T., Parsons, T., Powers, P. M., Shaw, B. E., Thatcher, W. R., Weldon, R. J., & Zeng, Y., 2014. Uniform California Earthquake Rupture Forecast, Version 3 (UCERF3)–The Time-Independent Model, *Bulletin of the Seismological Society of America*, **104**(3), 1122–1180.

Flück, P., Hyndman, R. D., & Wang, K., 1997. Three-dimensional dislocation model for great earthquakes of the Cascadia Subduction Zone, *Journal of Geophysical Research*, **102**(B9), 20539.

Hardebeck, J. L., 2010. Seismotectonics and Fault Structure of the California Central Coast, *Bulletin of the Seismological Society of America*, **100**(3), 1031–1050.

Hauksson, E., Yang, W., & Shearer, P. M., 2012. Waveform Relocated Earthquake Catalog for Southern California (1981 to June 2011), *Bulletin of the Seismological Society of America*, **102**(5), 2239–2244.

Hearn, E. H. & Thatcher, W. R., 2015. Reconciling viscoelastic models of postseismic and interseismic deformation: Effects of viscous shear zones and finite length ruptures, *Journal of Geophysical Research: Solid Earth*, **120**(4), 2794–2819.

Hetland, E. A. & Simons, M., 2010. Post-seismic and interseismic fault creep II: transient creep and interseismic stress shadows on megathrusts, *Geophysical Journal International*, **181**(1), 99–112.

Hetland, E. A., Simons, M., & Dunham, E. M., 2010. Post-seismic and interseismic fault creep I: model description, *Geophysical Journal International*, **181**(1), 81–98.

Hussain, E., Wright, T. J., Walters, R. J., Bekaert, D. P. S., Lloyd, R., & Hooper, A., 2018. Constant strain accumulation rate between major earthquakes on the North Anatolian Fault, *Nature Communications*, **9**(1), 1392.

Jiang, J. & Lapusta, N., 2016. Deeper penetration of large earthquakes on seismically quiescent faults, *Science*, **352**(6291), 1293–1297.

Johnson, K. M., 2013. Slip rates and off-fault deformation in Southern California inferred from GPS data and models, *Journal of Geophysical Research: Solid Earth*, **118**(10), 5643–5664.

Johnson, K. M. & Segall, P., 2004. Viscoelastic earthquake cycle models with deep stress-driven creep along the San Andreas fault system, *Journal of Geophysical Research: Solid Earth*, **109**(B10).

Johnson, K. M., Mavrommatis, A., & Segall, P., 2016. Small interseismic asperities and widespread aseismic creep on the northern Japan subduction interface, *Geophysical Research Letters*, **43**(1), 135–143.

Johnson, S. Y. & Watt, J. T., 2012. Influence of fault trend, bends, and convergence on shallow structure and geomorphology of the Hosgri strike-slip fault, offshore central California, *Geosphere*, **8**(6), 1632–1656.

Johnson, S. Y., Hartwell, S. R., & Dartnell, P., 2014. Offset of Latest Pleistocene Shoreface Reveals Slip Rate on the Hosgri Strike-Slip Fault, Offshore Central California, *Bulletin of the Seismological Society of America*, **104**(4), 1650–1662.

Lambert, V. & Barbot, S., 2016. Contribution of viscoelastic flow in earthquake cycles within the lithosphere-asthenosphere system, *Geophysical Research Letters*, **43**(19), 10,142–10,154.

Lin, G., Shearer, P. M., & Hauksson, E., 2007. Applying a three-dimensional velocity model, waveform cross correlation, and cluster analysis to locate southern California seismicity from 1981 to 2005, *Journal of Geophysical Research*, **112**(B12), B12309.

Mavrommatis, A. P., Segall, P., & Johnson, K. M., 2014. A decadal-scale deformation transient prior to the 2011 M w 9.0 Tohoku-oki earthquake, *Geophysical Research Letters*, **41**(13), 4486–4494.

Mavrommatis, A. P., Segall, P., & Kaj, J., 2017. A physical model for interseismic erosion of locked fault asperities, *submitted*.

Meade, B. J., Klinger, Y., & Hetland, E. A., 2013. Inference of Multiple Earthquake-Cycle Relaxation

Timescales from Irregular Geodetic Sampling of Interseismic Deformation, *Bulletin of the Seismological Society of America*, **103**(5), 2824–2835.

Nadeau, R. M. & Guilhem, A., 2009. Nonvolcanic Tremor Evolution and the San Simeon and Parkfield, California, Earthquakes, *Science*, **325**(5937), 191–193.

Noriega, G. R., Arrowsmith, J. R., Grant, L. B., & Young, J. J., 2006. Stream Channel Offset and Late Holocene Slip Rate of the San Andreas Fault at the Van Matre Ranch Site, Carrizo Plain, California, *Bulletin of the Seismological Society of America*, **96**(1), 33–47.

Obara, K., 2002. Nonvolcanic deep tremor associated with subduction in southwest Japan., *Science (New York, N.Y.)*, **296**(5573), 1679–81.

Savage, J. & Burford, R., 1970. Accumulation of tectonic strain in California, *Bulletin of the Seismological Society of America*, **60**(6), 1877–1896.

Savage, J. C., 1990. Equivalent strike-slip earthquake cycles in half-space and lithosphere-asthenosphere earth models, *Journal of Geophysical Research: Solid Earth*, **95**(B4), 4873–4879.

Savage, J. C. & Prescott, W. H., 1978. Asthenosphere readjustment and the earthquake cycle, *Journal of Geophysical Research: Solid Earth*, **83**(B7), 3369–3376.

Scharer, K., Weldon, R., Streig, A., & Fumal, T., 2014. Paleoearthquakes at Frazier Mountain, California delimit extent and frequency of past San Andreas Fault ruptures along 1857 trace, *Geophysical Research Letters*, **41**(13), 4527–4534.

Segall, P., 2010. *Earthquake and volcano deformation*, Princeton University Press, Princeton, New Jersey.

Segall, P. & Bradley, A. M., 2012. Slow-slip evolves into megathrust earthquakes in 2D numerical simulations, *Geophysical Research Letters*, **39**(18), 308.

Shelly, D. R., 2010. Periodic, Chaotic, and Doubled Earthquake Recurrence Intervals on the Deep San Andreas Fault, *Science*, **328**(5984), 1385–1388.

Shen, Z.-K., King, R. W., Agnew, D. C., Wang, M., Herring, T. A., Dong, D., & Fang, P., 2011. A unified analysis of crustal motion in Southern California, 1970-2004: The SCEC crustal motion map, *Journal of Geophysical Research: Solid Earth*, **116**(B11), n/a–n/a.

Sieh, K. E., 1978. Slip Along the San Andreas Fault Associated with the Great 1857 Earthquake, *Bulletin of the Seismological Society of America*.

Smith-Konter, B. R., Sandwell, D. T., & Shearer, P., 2011. Locking depths estimated from geodesy and seismology along the San Andreas Fault System: Implications for seismic moment release, *Journal of Geophysical Research*, **116**(B6), B06401.

Spiegelhalter, D. J., Best, N. G., Carlin, B. P., & van der Linde, A., 2002. Bayesian measures of model complexity and fit, *Journal of the Royal Statistical Society: Series B (Statistical Methodology)*, **64**(4), 583–639.

Takeuchi, C. S. & Fialko, Y., 2012. Dynamic models of interseismic deformation and stress transfer from plate motion to continental transform faults, *Journal of Geophysical Research: Solid Earth*, **117**(B5), n/a–n/a.

Wright, T. J., Elliott, J. R., Wang, H., & Ryder, I., 2013. Earthquake cycle deformation and the Moho: Impli-

cations for the rheology of continental lithosphere, *Tectonophysics*, **609**, 504–523.

Zhang, X. & Sagiya, T., 2018. Intraplate Strike-Slip Faulting, Stress Accumulation, and Shear Localization of a Crust-Upper Mantle System With Nonlinear Viscoelastic Material, *Journal of Geophysical Research: Solid Earth*, **123**(10), 9269–9285.

Zielke, O., Arrowsmith, J. R., Ludwig, L. G., & Akciz, S. O., 2010. Slip in the 1857 and Earlier Large Earthquakes Along the Carrizo Plain, San Andreas Fault, *Science*, **327**(5969), 1119–1122.

APPENDIX A: VISCOELASTIC STRESSES CAUSED BY REPEATED SLIP IN THE SEISMOGENIC REGION

Stress rates are obtained by computing the strain rates using velocities given in equation (2) and applying Hooke's law (Johnson & Segall 2004). Stresses are then derived by integrating over the duration of the time interval T. The expression for stress at the location (x_k, z_k) due to slip δ_i at depth z_i is

$$\sigma_i(x_k, z_k, t) = \delta_i \frac{\mu}{2\pi} \frac{T}{t_R} e^{-t/t_R} \sum_{n=1}^{\infty} \frac{W_n(x_k, z_k, z_i, H)}{(n-1)!} \sum_{k=0}^{K} e^{-kT/t_R} \left(\frac{t+kT}{t_R} \right)^{n-1}, \tag{A.1}$$

using the spatial operator W_n:

$$W_n(x_k, z_k, z_i, H) = V_n(x_k, z_k, z_{i+1}, H) - V_n(x_k, z_k, z_i, H), \tag{A.2a}$$

$$\text{where} \quad V_n(x_k, z_k, z_i, H) = -\frac{z_k - 2nH + z_i}{(z_k - 2nH + z_i)^2 + x_k^2} + \frac{z_k - 2nH - z_i}{(z_k - 2nH - z_i)^2 + x_k^2} \tag{A.2b}$$

$$+ \frac{z_k + 2nH + z_i}{(z_k + 2nH + z_i)^2 + x_k^2} - \frac{z_k + 2nH - z_i}{(z_k + 2nH - z_i)^2 + x_k^2}. \tag{A.2c}$$

For points on the fault, $x_k = 0$ and V_n simplifies to:

$$V_n(z_k, z_i, H) = -\frac{1}{z_k - 2nH + z_i} + \frac{1}{z_k - 2nH - z_i} + \frac{1}{z_k + 2nH + z_i} - \frac{1}{z_k + 2nH - z_i} \tag{A.3}$$

APPENDIX B: GENERALIZED EQUATIONS FOR CRACK MODEL

Following Bilby & Eshelby (1968), the stress drop within the crack can be expanded in Chebyshev polynomials of the first kind T_i:

$$\Delta\tau(u) = \mu \sum_{i=0}^{\infty} c_i T_i(u). \tag{B.1}$$

Bruhat & Segall (2017) showed that for a non-singular crack, i.e. with finite stress at the crack tip and driven by steady displacement δ^∞, $c_0 = 0$ and $c_1 = 2\delta^\infty / a\pi$. This leads to the following expressions

for stress drop within the crack and slip:

$$\Delta\tau(\xi,t) = \mu\frac{2\delta^\infty}{a\pi}\xi + \mu\sum_{i=2}^{\infty} c_i T_i(\xi), \tag{B.2}$$

$$s(\xi,t) = \frac{\delta^\infty}{\pi}\left[\xi\sqrt{1-\xi^2} + \arcsin(\xi) + \frac{\pi}{2}\right] + \frac{a}{2}\sqrt{1-\xi^2}\sum_{i=2}^{\infty} c_i\left[\frac{U_i(\xi)}{i+1} - \frac{U_{i-2}(\xi)}{i-1}\right]. \tag{B.3}$$

where U_i are Chebyshev polynomials of the second kind.

Finally, taking the total derivative of $s(\xi,t)$ to get slip-rate, I find

$$\frac{ds}{dt}(\xi,t) = \dot\delta^\infty g + \frac{a}{2}\sum_{i=2}^{\infty}\frac{dc_i}{dt}f_i + \frac{da}{dt}\left[g'\frac{1-\xi}{a}\delta^\infty + \sum_{i=2}^{\infty}\frac{c_i}{2}\Big(f_i + f_i'(1-\xi)\Big)\right], \tag{B.4}$$

where

$$f_i = \sqrt{1-\xi^2}\left[\frac{U_i}{i+1} - \frac{U_{i-2}}{i-1}\right], \tag{B.5a}$$

$$f_i' = 2\sqrt{1-\xi^2}U_{i-1}, \tag{B.5b}$$

$$g = \frac{1}{\pi}\left[\xi\sqrt{1-\xi^2} + \arcsin\xi + \frac{\pi}{2}\right], \tag{B.5c}$$

$$g' = \frac{2}{\pi}\sqrt{1-\xi^2}. \tag{B.5d}$$

APPENDIX C: TIME-DEPENDENT DISPLACEMENT CONDITION AT THE DOWN DIP LIMIT OF THE CRACK

Consider a 1D crack of length a in a full space loaded at displacement δ^∞(t) at the bottom end. The average long-term rate is v^∞ at depth. The medium is loaded at constant stress τ^∞. The stress acting on the fault is τ, such that the stress drop is defined as $\Delta\tau = \tau^\infty - \tau$. In this part, I describe how the bottom displacement and velocity conditions δ^∞(t) and $\dot\delta^\infty$(t) are computed such that they include time-dependent viscoelastic flow.

Equations (12.20)–(12.21) in Segall (e.g. 2010, Section 12.4.1) gives the horizontal velocity at the free surface due to the cumulative effect of N regularly spaced earthquakes:

$$v(x,t) = \frac{1}{\pi}\sum_{n=1}^{\infty}\mathcal{T}_n(t/t_R, T/t_R)\mathcal{F}_n(x,D,H), \tag{C.1}$$

where

$$\mathcal{T}_n(t/t_R, T/t_R) = \frac{v^\infty T}{t_R}\frac{e^{-t/t_R}}{(n-1)!}\sum_{i=0}^{N} e^{-kT/t_R}\Big(\frac{t+kT}{t_R}\Big)^{n-1}. \tag{C.2}$$

Savage (1990) noted that the viscoelastic solution given above is mathematically equivalent to fault slip within an elastic half-space in a series of strips at depths $H, 3H, ...$ below the coseismic region. Time dependence is then given by the term $\mathcal{T}_n(t/t_R, T/t_R)$. Since the crack bottom end lies

at the upper limit of the viscoelastic medium, the bottom velocity condition $\dot{\delta}^{\infty}$ corresponds to the velocity of the viscoelastic region at its upper end. In order to reproduce the time dependence of $\dot{\delta}^{\infty}$, I define it as a weighted sum of the first two nodes $\mathcal{T}_n$ from the previous equation. For large N, it can be rewritten as:

$$\dot{\delta}^{\infty}(t) = \frac{1}{2}\left[\mathcal{T}_1(t/t_R, T/t_R) + \mathcal{T}_2(t/t_R, T/t_R)\right] \quad \text{(C.3)}$$

$$= \frac{v^{\infty}T}{2t_R} e^{-t/t_R}\left(\frac{e^{-T/t_R}}{e^{-T/t_R}-1}\right)\left[1 + \frac{t}{t_R} + \frac{T}{t_R}\left(\frac{1}{e^{-T/t_R}-1}\right)\right] \quad \text{(C.4)}$$

This boundary condition has an exponential character and its average slip rate over the earthquake cycle is v^{∞}. Finally, I compute the condition δ^{∞} by numerical integration:

$$\delta^{\infty}(t) = \frac{1}{2}\int_0^t \left[\mathcal{T}_1(t/t_R, T/t_R) + \mathcal{T}_2(t/t_R, T/t_R)\right] dt. \quad \text{(C.5)}$$

APPENDIX D: EVALUATION OF CREEP-INDUCED VISCOELASTIC EFFECTS

In this section, I verify the method that I developed in section 2.3 against previous codes for creep-induced viscoelastic effects. I make use of earthquake cycle models developed by Johnson & Segall (2004) to compute slip-rate profiles for interseismic creep. This model assumes that the region between D and H is unlocked, is fixed in length during the interseismic period, and slips at constant resistive shear stress. The solution for slip and slip rate within the creeping region is then computed through a boundary element approach.

First I use profiles of surface rates and slip rates within the creeping region using the approach from Johnson & Segall (2004) to estimate the portion of surface deformation attributed to creep-induced viscoelastic response. For a given set of input parameters: rupture depth D, elastic thickness H, relaxation time t_R, recurrence time T, and plate motion velocity v^{∞}, I produce profiles of surface rates and interseismic slip rates. Here I use $D = 15$ km, $H = 30$ km, , $T = 300$ years, $v^{\infty} = 3$ cm/yr. Deformation profiles for two relaxation times t_R are displayed in figure A1. Left panels show profiles for surface rates and slip rates in the creeping region at ten time intervals during the interseismic period. These profiles are computed using codes from Johnson & Segall (2004). Top middle panel gives surface rates due to periodic earthquake rupturing from the surface to depth D every T years. These are computed using analytical solution for earthquake cycle models (as in Segall 2010, Section 12.4.2). Bottom middle panel displays elastic deformation rates caused by interseismic creep. These surface rates relate to the slip rates displayed in the bottom left panel via elastic Green's functions.

Right panels display the viscoelastic deformation as a function of time, and space, due to time-varying slip rate profiles shown in the bottom left panel. These profiles result from the subtraction

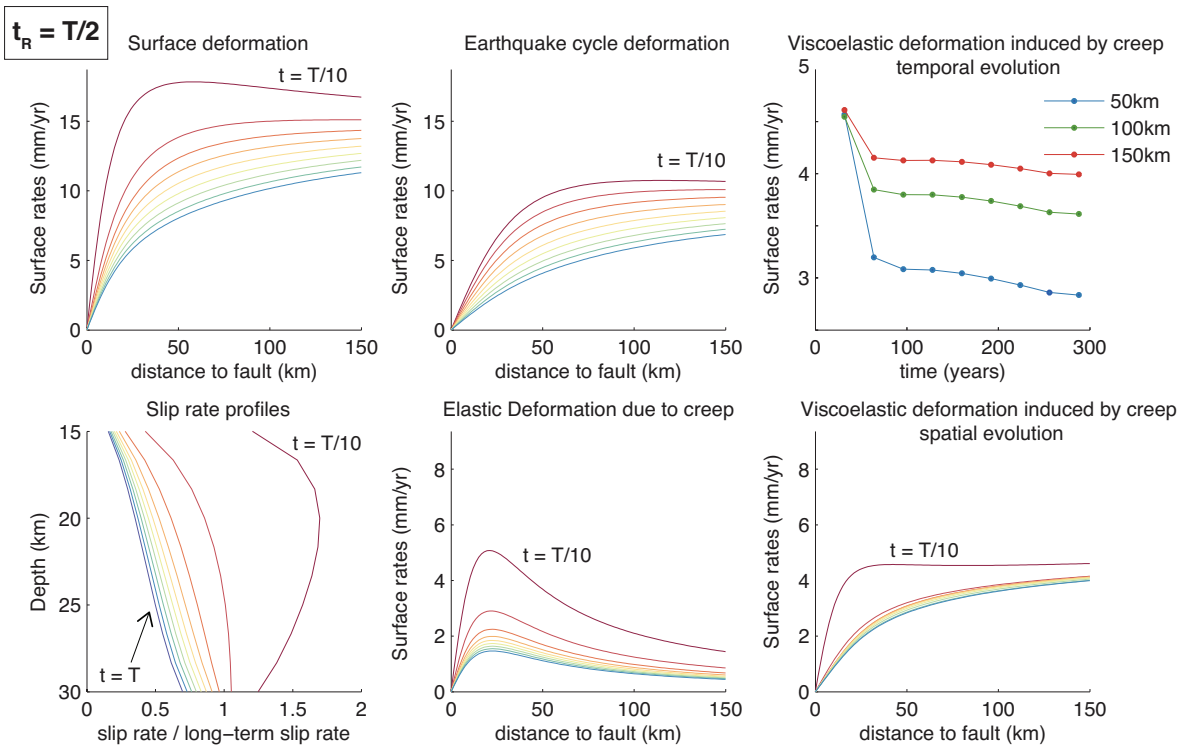

Figure A1. Estimation of viscoelastic deformation induced by time-varying creep when $t_R = T/2$. Left: profiles for surface rates and slip rates from Johnson & Segall (2004). Top middle: surface rates due to cyclic earthquake ruptures. Bottom middle: elastic rates caused by interseismic creep. Right: viscoelastic deformation as a function of time, and space, caused by slip rates in bottom left panel.

of the coseismic cycle deformation and the elastic deformation caused by creep, both displayed in middle panels, from the original surface deformation shown in the top left panel. Figure A1 shows that the surface deformation is dominated by the earthquake cycle signal, up to 70% of the signal. The amplitude of the elastic and viscoelastic deformation pattern are roughly similar, each accounting for 10–20% of the total rates. However, note the different evolution, as the elastic deformation decreases both temporally and spatially, while the viscoelastic response reaches an asymptotic trend which increases with distance from the fault. The viscoelastic signal will dominate especially late in the earthquake cycle. Since the viscoelastic effect of interseismic creep is comparable to the elastic part, I cannot neglect the effect of viscoelastic flow in the surface rates.

Now I compare the viscoelastic response induced by creep from Johnson & Segall (2004) with this model. I use the slip rate profiles of creep from Johnson & Segall (2004), considering 10 time increments, and compute the surface deformation from the viscoelastic response using equation (14) (see Figure A2). This method reproduces the overall shape and amplitude of the surface rates, especially late in the earthquake cycle. As I only use 10 increments in Johnson & Segall (2004)'s model,which is

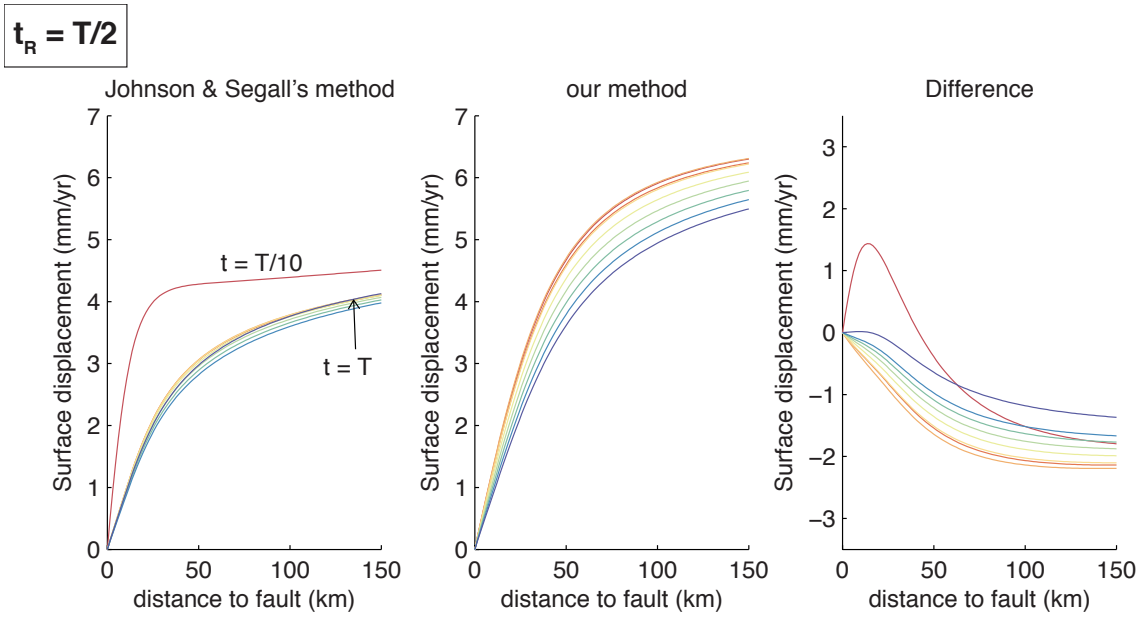

Figure A2. Surface predictions of viscoelastic deformation induced by time-varying creep using the method developed by Johnson & Segall (2004) and ours. The recurrence time is T = 300 years, $t_R = T/2$, and the number of time increments is 10.

the number of time increment used in the original paper, I now test the effect of increasing the number of time increments.

Figure A3 displays the misfit between the surface prediction from Johnson & Segall (2004) and this method as a function of the time discretization used in the boundary element code and time within the earthquake cycle. I show that the difference between the two methods decreases with finer discretization. The main difference lies in the earliest computed time. This corresponds to the instantaneous coseismic deformation in the creeping response, that appears in Johnson & Segall (2004)'s method, but not in mine. When used for later periods in the earthquake cycle, I conclude that this method is adequate enough to reproduce viscoelastic response induced by time-dependent creep. Obviously, one could advocate for using the method developed by Johnson & Segall (2004) with 10 and more time increments, but at that point the method becomes actually too computationally expensive to use in a MCMC context.

APPENDIX E: 3D EFFECTS

I use the kinematic block model developed by Johnson (2013) to compute 2D synthetic data along a line perpendicular to the Carrizo Plain section of the San Andreas fault (see Figure A4). This model considers the entire extent of the San Andreas fault in Central and Southern California. I assume the

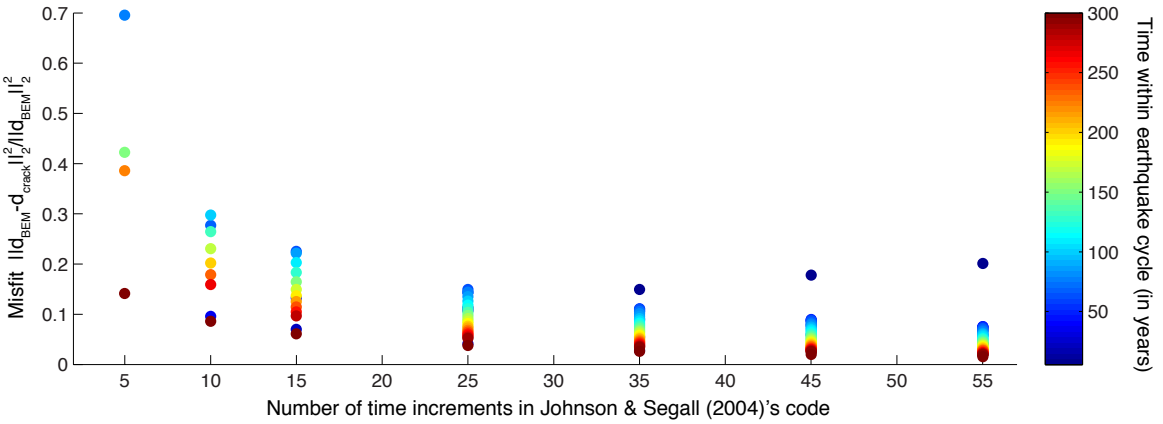

Figure A3. Comparison between the surface prediction of viscoelastic deformation induced by time-varying creep from Johnson & Segall (2004) (d_{BEM}) and this method (d_{crack}) as a function of the time discretization used in the boundary element code and time. The recurrence time is T = 300 years and $t_R = T/2$.

San Andreas fault locked up to 19 km (Smith-Konter et al. 2011) and fully creeping in the northern creeping section. Using the surface rates due to an infinitely-long fault also locked at 19 km, I compute the difference between the 1D and the 2D models that I considered as a correction to the surface rates. Corrected data are displayed in Figure 1.

[h]

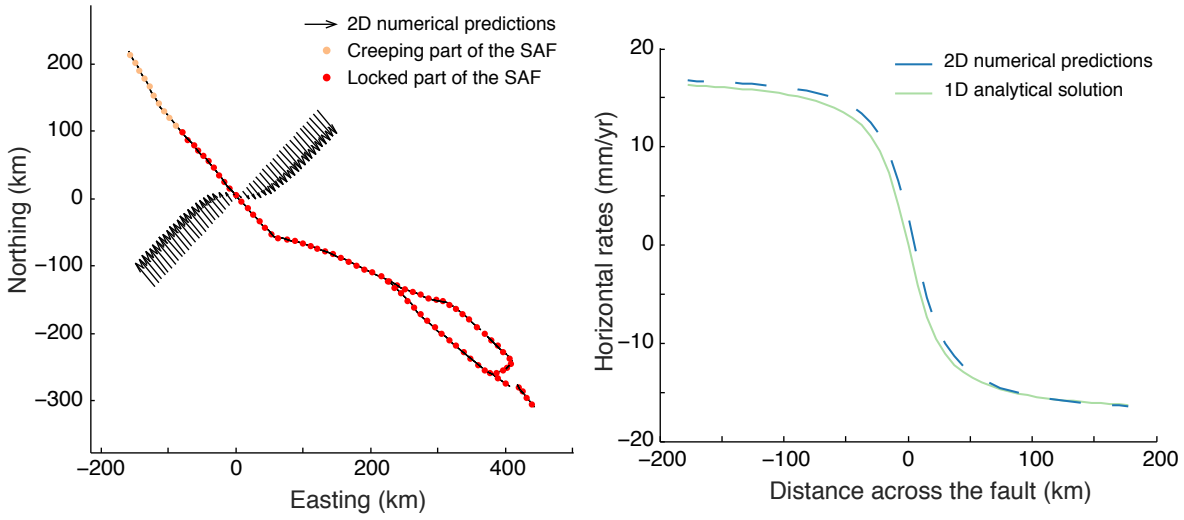

Figure A4. Estimation of 3D effects (locking depth is 19 km)

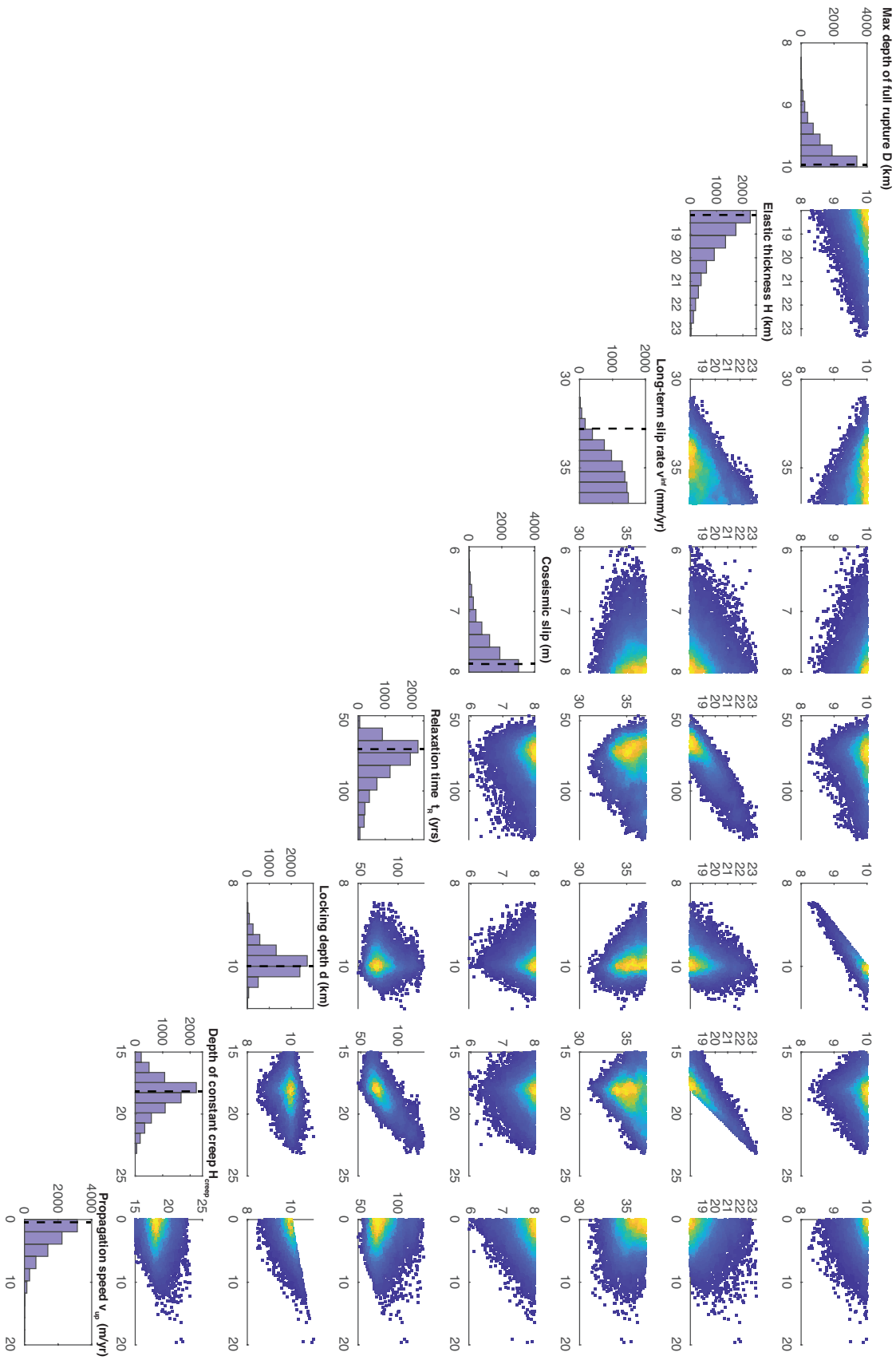

Figure A5. Marginal posterior distributions for parameters estimated in the propagating creep inversion. Best fitting solution are indicated by the dashed black lines.